Hindawi
International Journal of Aerospace Engineering
Volume 2023, Article ID 5520443, 21 pages
https://doi.org/10.1155/2023/5520443

Research Article

Numerical Simulations of Vertical Discrete Gusts Driven by Trailing Edge Blowing

Yang Shi, Bo Lu, Peng Guo, Binbin Lv, Hongtao Guo, and Li Yu

Institute of High Speed Aerodynamics, China Aerodynamics Research and Development Center, Mianyang 621000, China

Correspondence should be addressed to Li Yu; yuli@cardc.cc

Received 14 May 2023; Revised 25 November 2023; Accepted 27 November 2023; Published 20 December 2023

Academic Editor: Vijayanandh Raja

A new type of gust generator generates the airflow oscillation in the wind tunnel through the Coanda effect of the unsteady trailing edge blowing, which has been shown to have strong potential for accurately simulating discrete gusts. It is necessary to study the relationship between the generated gust characteristics and the control parameters of such devices in order to optimize the design performance and improve gust simulation capabilities. By solving the compressible unsteady Reynolds-averaged Navier–Stokes (URANS) equations, the computational fluid dynamics model of the subsonic airflow past the gust generator in the wind tunnel was presented. The effects of jet momentum, frequency, and spanwise blowing ratio on gust intensity, shape, and spatial uniformity were investigated. Results indicate that the intensity of gusts is positively correlated with jet momentum and frequency. The gust shape matches well with the normalized jet momentum coefficient curve. However, when the frequency increases to above 10 Hz, the gust shape differs significantly from expectation due to the appearance of reverse wave peaks. In addition, the mechanism of the impact of the sidewall and partial spanwise blowing on gusts was revealed. In the three-dimensional situation, streamwise vortices are formed on the sidewall and at the spanwise position where the blowing stops, respectively. This results in an increase and noticeable nonuniformity in gust amplitude. When the blowing with a 15% spanwise length near the sidewall is turned off, the gust amplitude at the symmetry plane increases by nearly 40% due to the main vortex being closer to the main flow. The result provides a physical explanation for the availability of this operation to reduce gust attenuation.

1. Introduction

During the flight, the aircraft is often subjected to the sudden change of aerodynamic load caused by gusts, which leads to some problems [1]. For example, the aircraft can be difficult to operate, the structure may be at risk of damage, and the comfort of passengers is reduced. This complex atmospheric phenomenon is usually manifested as instantaneous or continuous changes in wind speed and direction, and the additional aerodynamic load causes wing vibration and fuselage shaking. The wing structure of modern aircraft is designed to have low weight and great flexibility. Large aircraft such as modern large-scale passenger aircraft, transport aircraft, and high-altitude long-endurance unmanned aerial vehicles are more sensitive to gusts. In recent years, the research on gust response and load alleviation of aircraft has become one of the hotspots in aeroelasticity [2]. Predicting the dynamic response caused by gusts and introducing corresponding control measures to reduce the load have become very important issues in the design of modern large aircraft.

With the development of gust simulation technology in wind tunnels, researchers can conduct accurate gust response evaluation and load alleviation system tests in the early design stage [3, 4]. In addition, high-quality wind tunnel verification data can be used to improve the numerical codes, thus further reducing the time cost of aircraft development in the long run. At present, some low-speed wind tunnels are equipped with gust generator devices, and they generate periodic disturbances with different frequencies and amplitudes through oscillating cascades [5, 6] or rotating components [7] located upstream of the test section. For high-speed wind tunnels, there are only a handful of facilities equipped with corresponding simulation technologies. The DNW-TWG wind tunnel of the German Aerospace Center

(DLR) [8] and the S3Ch wind tunnel of the French Aerospace Lab (ONERA) [9] both adopt the gust generators of oscillating cascades. And gusts are formed by the wake vortices created by the pitch motion of these cascades. However, due to the large size of the cascades traversing the test section and the limited power of the actuators, this form is not appropriate for large-scale transonic wind tunnels. The system utilizes oscillating wingtip vortices to generate gusts in the Transonic Dynamic Tunnel (TDT) of NASA Langley Research Center, which is the earliest high-speed facility to carry out gust response tests. The size of the test section is $16\,\text{ft} \times 16\,\text{ft}$, and its gust generator consists of two groups of oscillating vanes mounted on the side walls [10], as shown in Figure 1. A flow angle variation of approximately $\pm 1^{\circ}$ can be provided in the region of the model by running the two pairs of vanes simultaneously [11]. These devices that generate disturbance to the stream flow by means of vanes or cascade oscillation have the advantages of simple structure, convenient control, and clear gust generation mechanism, while small frequency coverage and single gust shape (sinusoidal) become the limits. Additionally, due to the power limitations of the driving methods, the generation of individual discrete gusts under subsonic and transonic flow through these devices seems to be a challenging task [12], even though this is precisely the gust profile required for airworthiness certification.

In recent years, the circulation control method has been used in many practical situations, benefiting from the precise and effective control capabilities. These situations cover not only flow control or lift enhancement [13, 14] but also new applications such as flight control and load alleviation [15, 16]. With the development of unsteady trailing edge blowing control methods [17], researchers designed a new type of gust generator based on the concept of circulation control, to avoid unacceptable vibration in the wind tunnel structure and achieve precise control of gust characteristics. Allen and Quinn [18] and Gomariz-Sancha et al. [19] reported the researches about the development and testing of the gust rig in the transonic wind tunnel (TWT) of Aircraft Research Association Ltd. (ARA). The scheme is based on two vanes vertically mounted in the contraction section, with a directional controllable blowing jet on the top and bottom of the trailing edge. Figure 2 shows the internal structure of a single vane. The accurate simulation of the gust profile can be achieved by controlling the solenoid valves on the airflow paths inside the vanes. This gust rig of TWT can generate discrete gusts with "1-cos" profile through trailing edge blowing, which is consistent with the gust model selected in mainstream airworthiness regulations [20, 21]. It enables wind tunnel testing to provide direct and effective gust load data for aircraft certification. In addition, this gust rig has high flexibility in the shape, intensity, and duration of gusts, allowing data to be acquired for the testing of novel load alleviation methods as well as the validation of computational methods.

However, it is difficult to find relevant research results on the mechanism of gust generation using trailing edge blowing in public literature. The two relevant reports [18, 19] did not address detailed information on the impact of jet parameters on gust characteristics. This cannot provide sufficient guidance for the promotion and performance optimization of such devices. Although using the research results of circulation control airfoil for reference helps to increase understanding of the operational characteristics of the gust generator, there are still some differences between them. Studies about the circulation control airfoil mainly focus on the lift and drag variation caused by jets [14], while the gust generator is designed to induce the deflection of the downstream flow with little consideration for the aerodynamic characteristics of the vane.

In order to generate high-quality and standardized discrete gusts in wind tunnels, it is necessary to conduct numerical research to fill the research gap in the mechanism of gust generation driven by trailing edge blowing. Therefore, this work attempts to simulate the unsteady flow over the gust generator in the wind tunnel to verify the effectiveness of this method and obtain the basic characteristics of gusts. In addition, Nishino and Shariff [22] have demonstrated that the unexpected formation of streamwise vortices around the junctions of the airfoil model and the sidewall can lead to differences between two-dimensional (2D) and three-dimensional (3D) solutions. The differences include not only the difference in gust amplitude on the symmetry plane but also the spatial nonuniformity in 3D solutions. And the spanwise nonuniform discrete gusts have been shown to have a significant impact on the gust response of high aspect ratio aircraft [23]. Some gust disturbances with specific spanwise distributions will cause more severe structural vibrations and critical loads than uniform gusts [24]. More precise evaluation of the dynamic gust response of aircraft can be achieved by examining the impact of jet parameters on spanwise distribution. Furthermore, in 3D situations, the spanwise blowing ratio becomes another key control parameter. In Ref. [19], it was mentioned that opening only 70% of the jet can effectively resist gust attenuation, but the availability of this method did not get clarified. So, we also investigate how the spanwise blowing ratio affects gust characteristics while considering the sidewall of the wind tunnel test section. The previous part of this research demonstrates that the basic characteristics of gusts are closely related to the jet momentum coefficient, and the influence pattern is revealed. In the latter part of this study, the general mechanism of sidewall effect is determined by the analysis of differences between 2D and 3D solutions. Additionally, partially closing the spanwise blowing can effectively increase the gust amplitude in the mainstream region due to the formation of the large streamwise vortex. The results of this study provide some useful guidance and suggestions for the design and operation of the trailing edge blowing gust generator for high-speed wind tunnels.

2. Methods

2.1. Model Geometry. According to Ref. [19], the basic configuration of the research model section adopted is a 2D symmetrical vane shape as shown in Figure 3, where c is the chord length, and the max thickness is $0.2c$. The middle sections are connected by straight lines, and the leading and trailing edges are hyperelliptic curves, with an index of 2.25

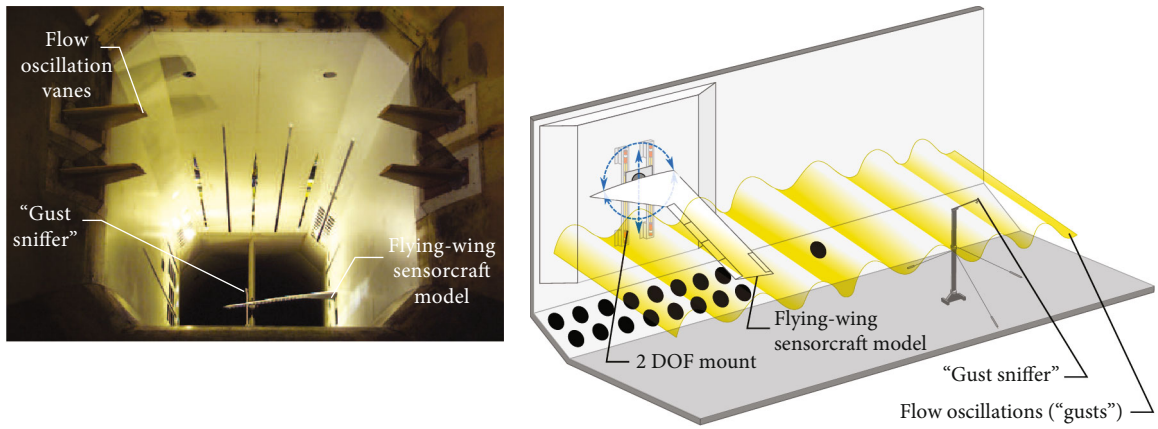

(a) The gust generator (b) The test model encountering gusts

Figure 1: The gust response test system of TDT [11].

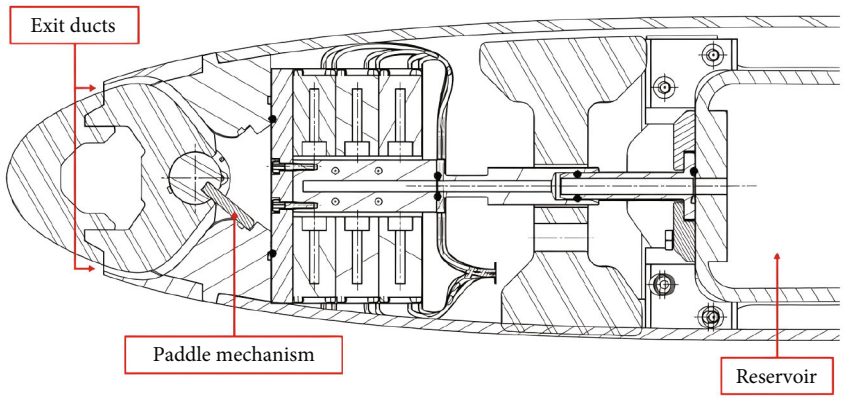

Figure 2: Internal structure of the gust generator device of TWT [19].

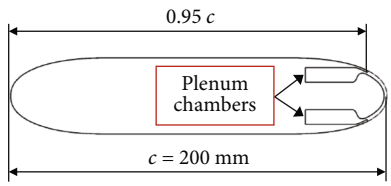

Figure 3: Model geometry of the trailing edge blowing vane section.

and a length of 0.25c. The jet slots are set at 0.95c, while the height is equal to the lip thickness, 0.005c. After being modified, the chord length of the vane changes to 0.9925c. Through a contraction pipeline, one plenum chamber is connected to each jet slot, and the height at the exit is the minimum. The trailing edge after the jet exit is also a super-elliptical line, which is the profile of the basic configuration trailing edge after scaling. The tangent slope of the path surfaces at the exit and the external surface are consistent. The tail profile and the contraction path are smooth and continuous at the slot. In addition, only the top jet is working as the goal of this study is to simulate vertical discrete gusts.

2.2. Numerical Method and Grids. It is pointed out in Ref. [25] that more flow details on the Coanda surface are presented by large eddy simulation (LES), thus improving the ability to predict jet separation. However, for this study, the main focus is on the wake flow and large-scale vortices rather than small-scale turbulent structures. Due to the relatively large computational domain, it is expensive to conduct 3D LES simulations for this problem. Previous studies have confirmed that the unsteady Reynolds-averaged Navier–Stokes (URANS) equation, combined with appropriate turbulence models, can accurately reflect the separation behavior of the jet on the curved surface. Nishino and Shariff [22] performed 3D simulations of circulation control airfoil with sidewall using the URANS approach and shear stress transport (SST) turbulence model. In addition, the conclusion in Ref. [25] shows that the introduction of curvature correction can greatly improve the reliability of the RANS equation in estimating the jet's separation position. Therefore, in this study, the compressible URANS equation is selected as the governing equation, and the $k-\omega$ SST model with rotating and curvature correction is selected as the turbulence model [26]. In this model, the factor F_4, related to the flow curvature, is introduced into

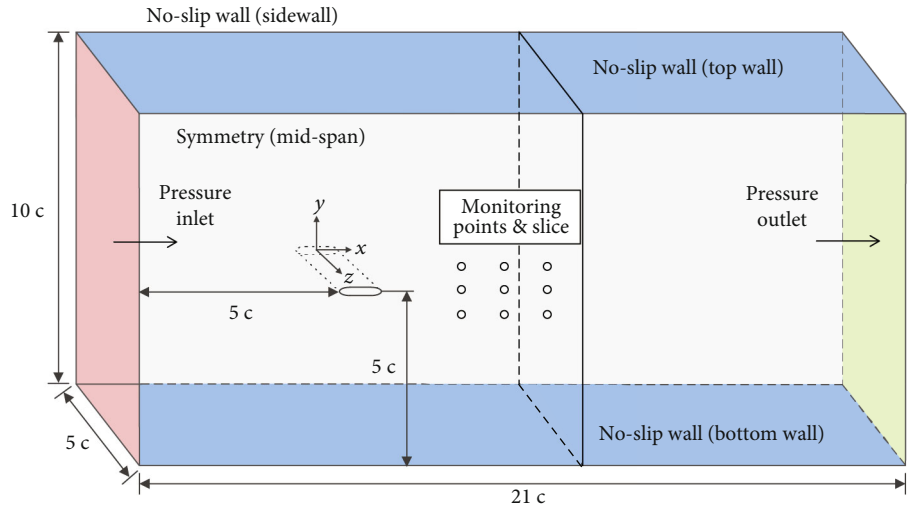

Figure 4: Schematic diagram of the calculational domain and boundary conditions.

Table 1: Results of the gird independence study.

Grid	Vane surface nodes	Trailing edge nodes	Wake streamwise nodes	C_L	Y velocity (m/s)
Coarse	201	101	51	0.252	-2.024
Medium	301	151	101	0.231	-1.515
Fine	401	201	151	0.228	-1.498

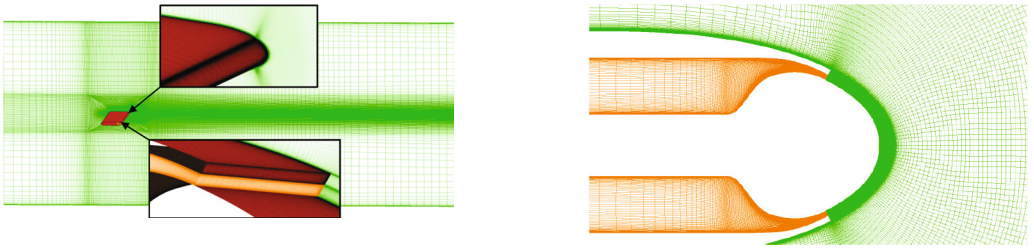

(a) Mesh of the symmetry plane and details near the trailing edge and jet slot (b) Mesh details of the plenum chambers

Figure 5: Grid distribution in 3D simulation.

the ω-equation. The equations and the factor's expression are as follows:

$$\rho\frac{\partial k}{\partial t}+\rho u_j\frac{\partial k}{\partial x_j}=P-\beta^*\rho k\omega+\frac{\partial}{\partial x_j}\left[\left(\mu+\frac{\mu_t}{\sigma_k}\right)\frac{\partial k}{\partial x_j}\right], \quad (1)$$

$$\rho\frac{\partial \omega}{\partial t}+\rho u_j\frac{\partial \omega}{\partial x_j}=\frac{\gamma\rho}{\mu_t}P-F_4\beta\rho\omega^2+\frac{\partial}{\partial x_j}\left[\left(\mu+\frac{\mu_t}{\sigma_\omega}\right)\frac{\partial \omega}{\partial x_j}\right]+2\rho\frac{1-F_1}{\sigma_{\omega 2}\omega}\frac{\partial k}{\partial x_j}\frac{\partial \omega}{\partial x_j}, \quad (2)$$

$$F_4=\frac{1}{1+C_{rc}R_i}. \quad (3)$$

The value of constant C_{rc} is 1.4 for all simulations in this study, according to the previous recommendations [25, 27]. For details on other terms in the equations, refer to Ref. [26]. The spatial discretization follows the second-order upwind scheme, and the temporal discretization is the second-order implicit scheme in the transient calculation. The calculational region and boundary conditions are presented in Figure 4. Pressure inlet and outlet conditions are used for external flow inlet and outlet, respectively. The no-slip wall conditions are set to simulate the test section walls. However, in the current study, the symmetric boundary is used at the middle span to save computational costs. As mass flow control is the most common means of jet control in experiments, the mass flow rate inlet conditions are selected on the left side of the plenum chambers to adjust jet parameters.

In the first part of this paper, the 2D flow over the gust generator is simulated for parametric research without

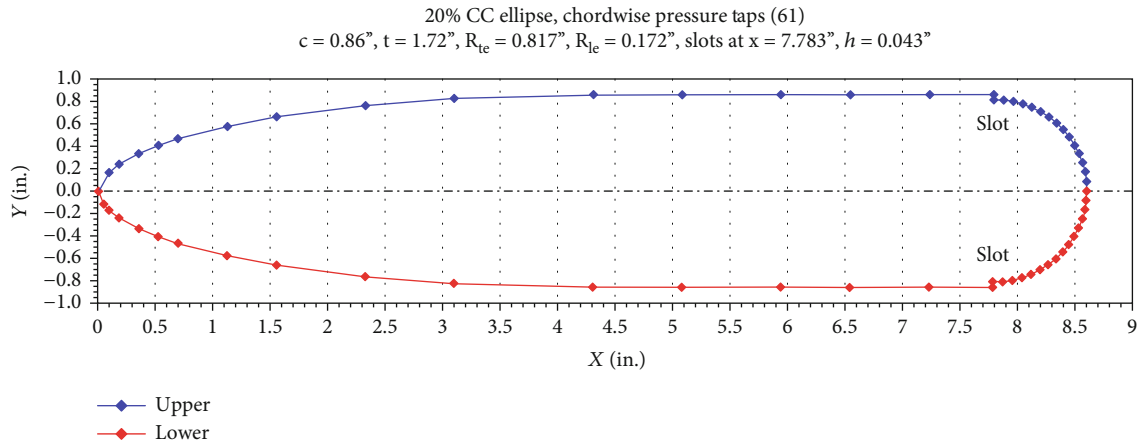

(a) CC020-010EJ circulation control airfoil profile [28]

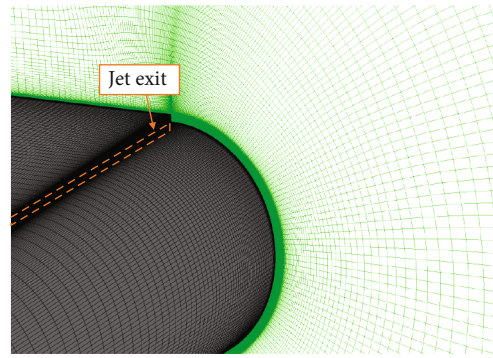

(b) Details of the 3D mesh

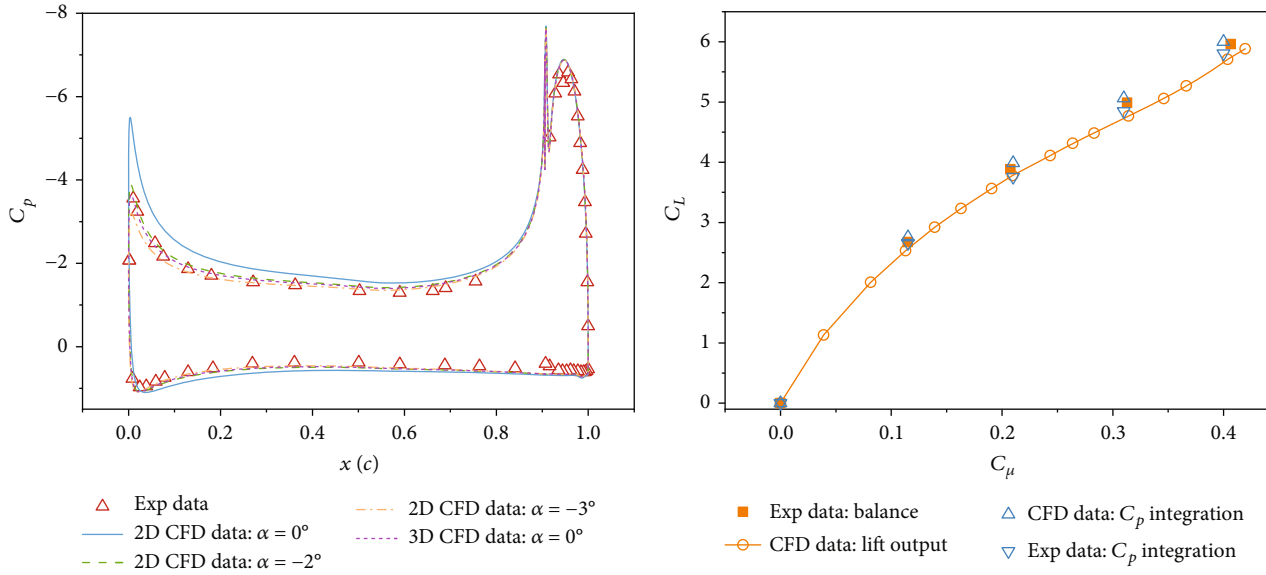

(c) The pressure coefficient distribution data

(d) The lift coefficient data

Figure 6: The airfoil profile, mesh, and results of numerical method validation.

considering the tunnel sidewall. In the latter part, 3D simulations are carried out to investigate the influence of the sidewall and spanwise blowing ratio on gusts and the features of spanwise distribution. Therefore, in this work, 2D and 3D structured meshes of the computational domain are used, while the 3D mesh is formed by extending the 2D mesh along the spanwise direction. Three 2D meshes with different grid resolutions are compared to determine the appropriate grid division. Their difference lies largely in the number of grid nodes on the trailing edge profile and downstream flow field near the vane in the streamwise direction ($1.5c < x < 6c$). The comparison results are presented by the

Table 2: 2D steady case description.

Case	$\dot{M}_{2D}$ (kg/s)	C_μ	p_{0j}/p_∞	Case	$\dot{M}_{2D}$ (kg/s)	C_μ	p_{0j}/p_∞
1	0.1479	0.0102	1.0935	8	0.3003	0.0480	1.4964
2	0.1878	0.0168	1.1511	9	0.3121	0.0506	1.5540
3	0.2184	0.0233	1.2086	10	0.3240	0.0530	1.6115
4	0.2421	0.0289	1.2662	11	0.3355	0.0553	1.6691
5	0.2607	0.0349	1.3237	12	0.3472	0.0575	1.7266
6	0.2758	0.0401	1.3813	13	0.3589	0.0597	1.7842
7	0.2885	0.0450	1.4388	14	0.3706	0.0618	1.8417

lift coefficient of the vane and the y velocity at a point ($x = 5c$, $y = 0$) under medium blowing condition, as shown in Table 1. Considering the overall quantity, scale, and calculation cost of 3D simulations, we choose the medium mesh for 2D simulations, where the vane surface is divided into 301 nodes and the trailing edge curve is divided into 151 nodes, as shown in Figure 5. The grids near surfaces and walls are refined to simulate the flow in the boundary layer, and the first grid distance is kept so that $y+$ can meet the requirements of the turbulence model. In addition, the size of grids in the wake area is controlled to capture the unsteady jet path. The 2D and 3D meshes consist of about 0.15×10^6 quads and 12×10^6 hexes, respectively.

There is little sufficient gust data to conduct numerical method verification owing to an incomplete description of the geometry parameters and experimental results of the trailing edge blowing gust generator in the previous literature. This paper performs 2D and 3D validations of the circulation control airfoil according to Ref. [28]. Figures 6(a) and 6(b) show the profile of the benchmark airfoil CC020-010EJ and the mesh for simulation. Figure 6(c) presents the comparison between the surface pressure coefficient distribution data measured in the wind tunnel test and the simulation results of the 2D and 3D validations in this study. In the 2D CFD result of 0° angle of attack, the data near the airfoil tail are highly consistent, but the simulation results at the leading edge exceed the experimental data. This is because the juncture flow on the model and sidewalls in the test section leads to a downwash on the airfoil, thus reducing the effective angle of attack in the wind tunnel. Then, correction simulations of -2° and -3° are carried out, respectively. The data nearing the leading edge at -2° agree well with the experimental results, which supports the conclusion in Ref. [28]. At the same time, the midspan data of 3D simulation is in good agreement with the test results. In addition, the lift coefficient results under different blowing conditions are compared, as shown in Figure 6(d). The two sets of experimental data in the figure are obtained from the balance record and the pressure coefficient integration. So, we also plot two sets of CFD data: the integrated midspan pressure coefficient results and direct lift output. The comparison shows that the simulation results and experimental results agree well. As a result, the availability of the numerical method is confirmed.

2.3. Case Description. The ultimate aim of this study is to improve the simulation ability of discrete gusts in wind tunnels, so the simulation object is the "1-cos" gust model used in mainstream airworthiness regulations [20]. Due to the vertical symmetry, only the upper jet is open in simulations. The unsteady inlet condition is set to follow a similar profile, according to Eq. (4). In this formula, $\dot{M}$ and f represent the amplitude of mass flow rate and the inverse of discrete gust duration. t_0 is 0.05 s for 2D cases and 0.01 s for 3D cases as the starting time of the internal flow.

$$\dot{m} = \begin{cases} \dfrac{\dot{M}}{2}\left(1 - \cos\left(2\pi f t\right)\right), & t_0 \le t \le t_0 + \dfrac{1}{f} \\ 0, & t < t_0, \le t_0 + \dfrac{1}{f} \end{cases}. \tag{4}$$

Similar to the research of circulation control airfoils, this study also uses the momentum coefficient at the slot, C_μ, to describe the jet intensity, calculated according to

$$C_\mu = \frac{F_j}{q_\infty A} \approx \frac{\dot{m}_j u_j}{q_\infty A}, \tag{5}$$

$$u_j = \sqrt{\frac{2\gamma}{\gamma - 1} R T_{t,j}\left(1 - \left(\frac{p_j}{p_{t,j}}\right)^{(\gamma-1)/\gamma}\right)}, \tag{6}$$

where F_j, $\dot{m}_j$, u_j, q_∞, and A represent the thrust generated by blowing, the jet mass flow rate, the flow velocity at the jet exit, the dynamic pressure of the incoming flow, and the area of the jet slot. In the experiment, the jet velocity is generally calculated through the isentropic expansion relation, such as Eq. (6). Then, C_μ is determined by the measured jet mass flow rate. In the equation, γ, R, $T_{t,j}$, $p_{t,j}$, and p_j represent the specific heat ratio, gas constant, total jet temperature, total pressure, and static pressure at the jet slot, respectively. In some work, p_j is calculated as the static pressure of the incoming flow. But during blowing, the actual static pressure is lower than that of the incoming flow, which will lead to the inadequate prediction of the jet velocity [28].

Tables 2 and 3 list the internal flow inlet conditions employed in 2D cases, and Table 4 lists the conditions in 3D cases. In 2D simulations, there are 14 steady cases of different mass flow rate conditions. The corresponding jet momentum coefficients are calculated by substituting the flow field data at the slot into Eq. (5), with the specific range

Table 3: 2D unsteady case description.

Case	$\dot{M}_{2D}$ (kg/s)	f (Hz)	Case	$\dot{M}_{2D}$ (kg/s)	f (Hz)
15	0.2421	5	21	0.2885	5
16	0.2421	10	22	0.2885	10
17	0.2421	20	23	0.2885	20
18	0.2758	5	24	0.3240	5
19	0.2758	10	25	0.3240	10
20	0.2758	20	26	0.3240	20

Table 4: 3D unsteady case description.

Case	$\dot{M}_{3D}$ (kg/s·m)	f (Hz)	Blowing activation ratio	Case	$\dot{M}_{3D}$ (kg/s·m)	f (Hz)	Blowing activation ratio
39	0.2758	5	100%	42	0.2421	10	100%
40	0.2758	10	100%	43	0.3240	10	100%
41	0.2758	20	100%	44	0.2758	10	85%

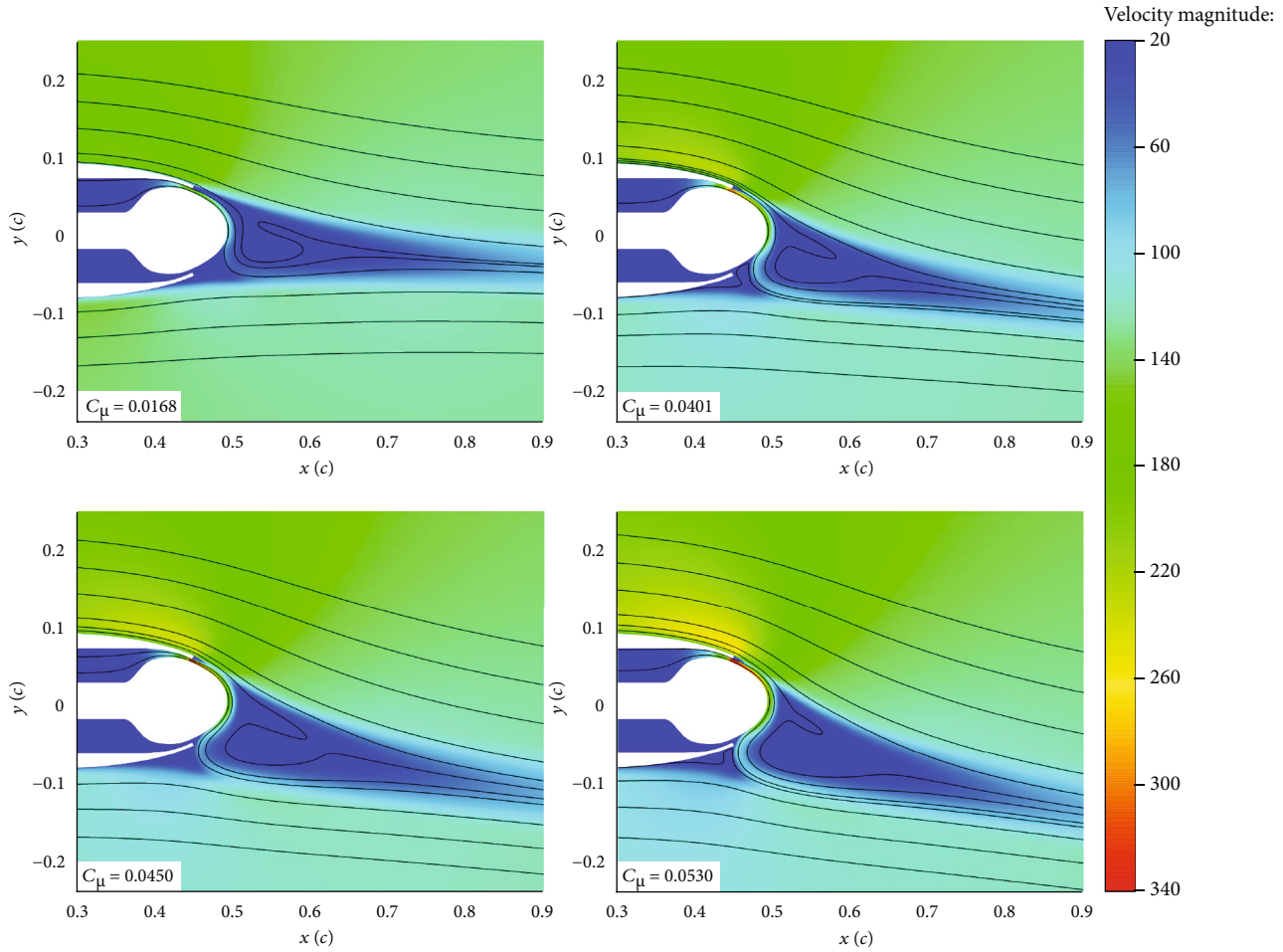

Figure 7: Velocity contours and streamlines of steady jet cases.

being 0.0102 to 0.0618. The steady simulations are performed here to illustrate the basic flow characteristics under various jet momentum coefficients and provide reference values for the comparative analysis of unsteady solutions. Unsteady cases 15~26 are simulations of discrete gusts. The values of mass flow rate amplitude are selected from inlet conditions of four steady cases. The durations of discrete gusts are 0.05 s, 0.1 s, and 0.2 s. For the convenience

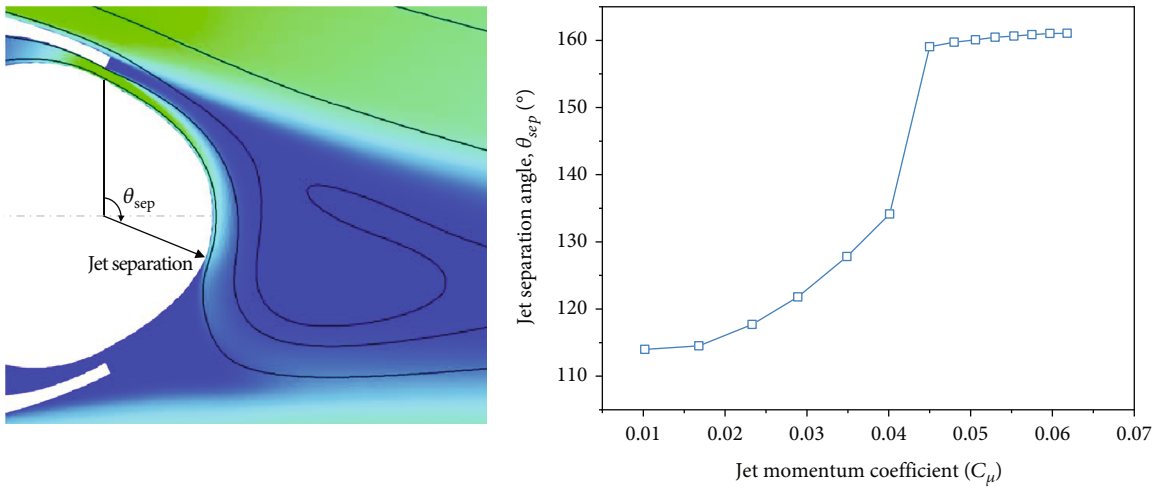

(a) Schematic diagram of jet separation angle

(b) Variation of jet separation angle

Figure 8: Characteristics of jet separation angle.

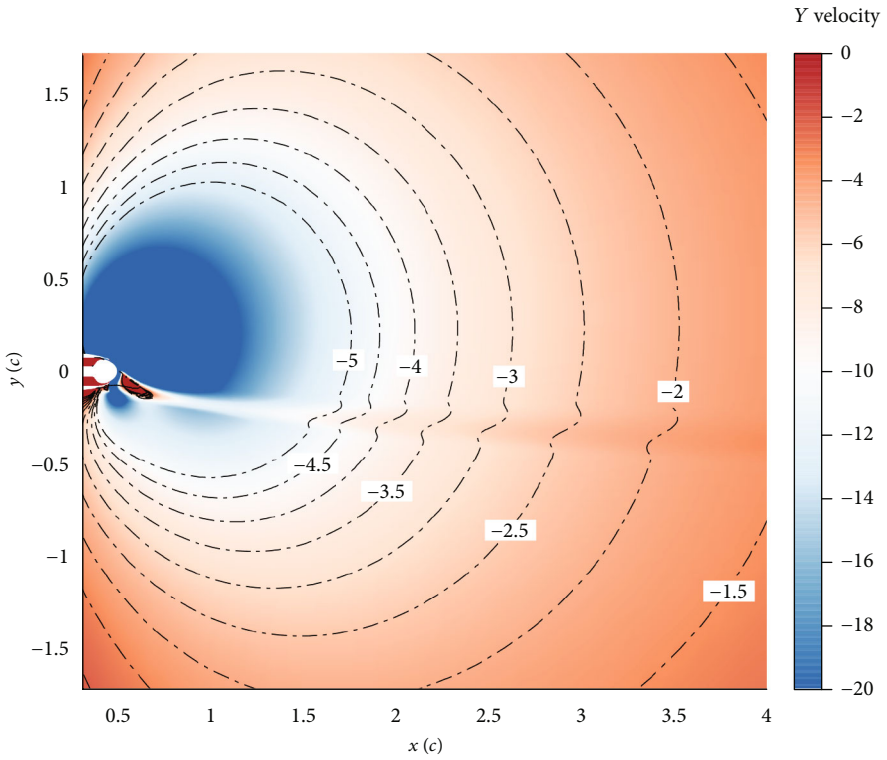

Figure 9: Contour of vertical velocity and isolines of gust angle.

of expression, frequency is used to refer to the duration. There are 6 different conditions to study the effects of sidewall and spanwise blowing activation ratio on gusts in 3D simulations. The blowing activation ratio in the table refers to the ratio of the spanwise length of the jet-opening region to the vane's span length. The purpose of the last case is to explain and study the behavior in the report [19], which is to only activate a portion of the spanwise jet to prevent rapid attenuation of the gust. Considering that the typical half-model or full-model spanwise length can reach 50% to 60% of the test section width, an activation ratio of 85% is selected as the comparison condition to ensure that the gusts generated in the model area are in phase. It should be noted that when setting the inlet condition of internal flow in the 3D case, the amplitude of the mass flow rate $\dot{M}$ in the corresponding 2D case needs to be multiplied by the active spanwise length. For all cases, the incoming Mach number is 0.4, the total pressure is 97 kPa, the total temperature is 288 K, and the chord-based Reynolds number is 1.6648×10^6.

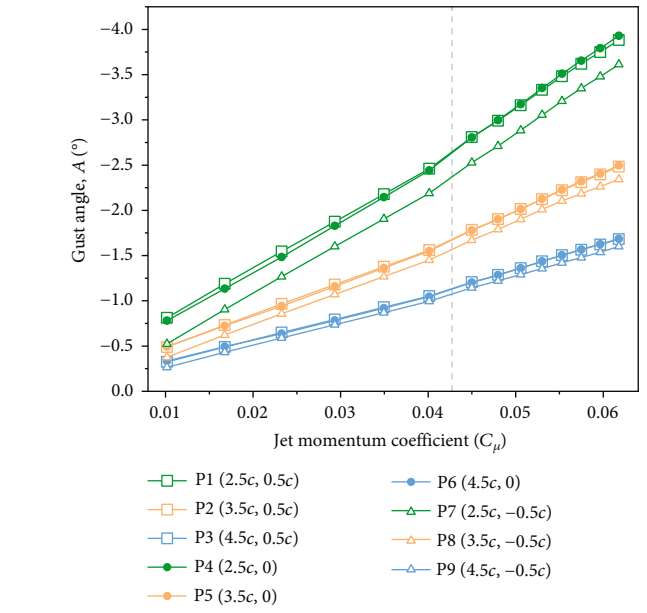

(a) Overall variation

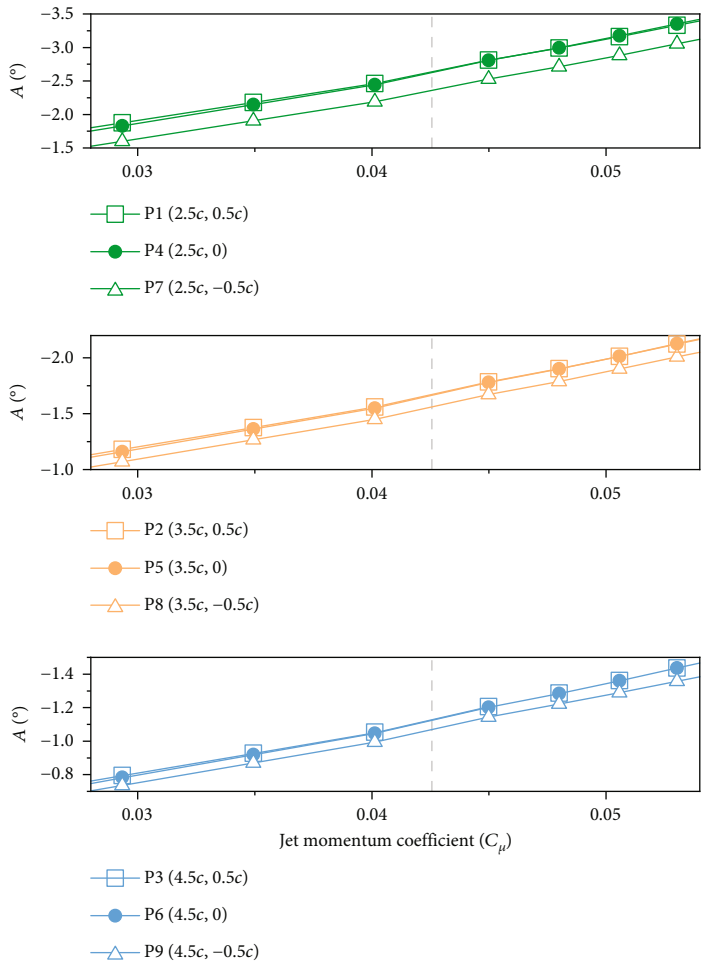

(b) Partially enlarged view

Figure 10: Variation of gust angle with jet momentum coefficient.

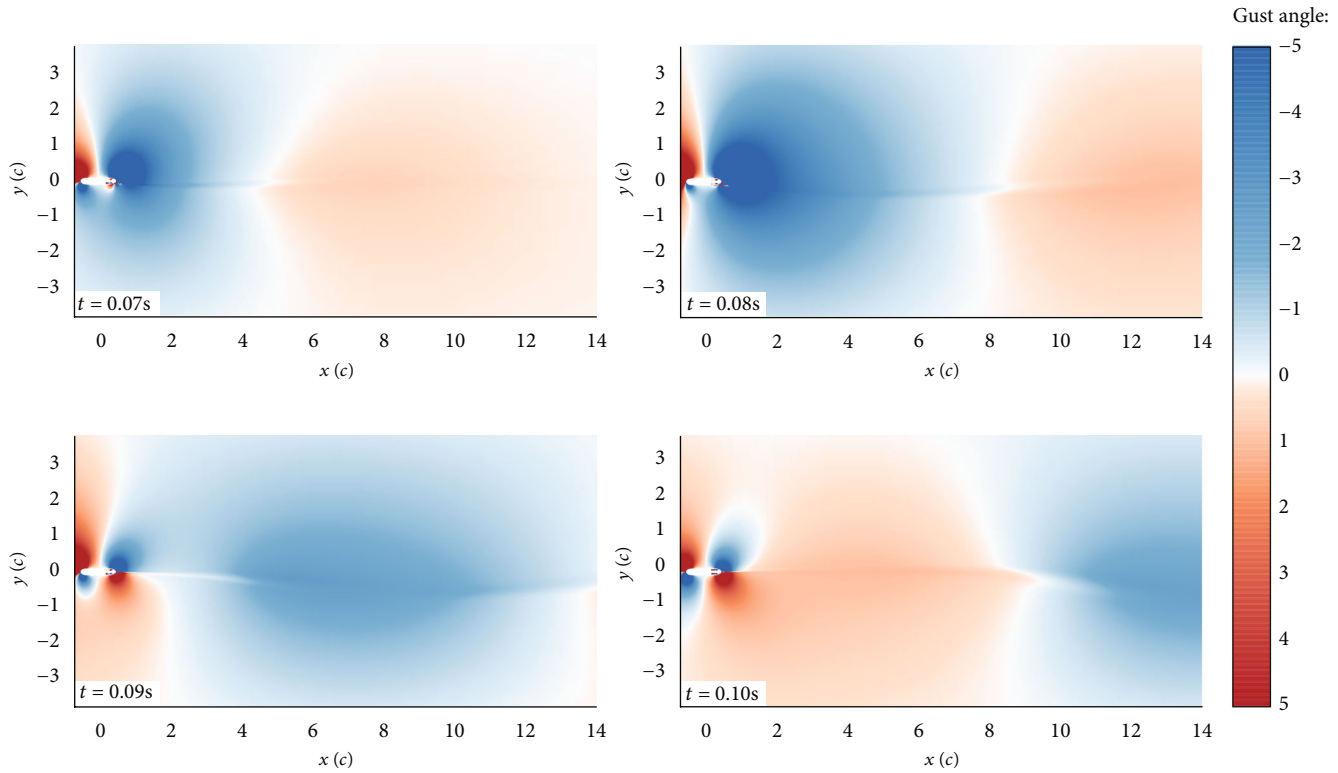

Figure 11: Transient contours of gust angle in case 23.

All 2D and 3D unsteady simulations take the steady solutions without blowing as the initial conditions to save calculation time. The time step of $\Delta t = 1/1000f$ and 20 internal iterations is adopted in the computations, where the definition of f is consistent with the above, the inverse of duration for discrete gusts.

3. Results and Discussion

3.1. Results without Wind Tunnel Sidewalls

3.1.1. Steady Jet Results. The velocity contour and streamlines of the downstream flow field in some typical steady cases are displayed in Figure 7. It can be seen from the streamline distribution that both upper and lower mainstreams deflect downward, and the deflection angle increases with the jet momentum coefficient. The separation angle of the jet is an important indicator in the study of the Coanda flow [25], as shown in Figure 8(a). The variation of jet separation angle under various operating conditions is displayed in Figure 8(b). It can be found that when C_μ is small, the jet will separate before contacting the vane's lower surface. The jet separation position moves down continuously, and the separation angle increases as C_μ rises. When C_μ reaching 0.0401~0.045, the separation angle increases sharply. Subsequently, the separation position of the jet remains basically unchanged.

To evaluate the jet effect on downstream flow more effectively, flow angle A is taken as the evaluation reference of flow deflection. In unsteady cases, it is also called gust

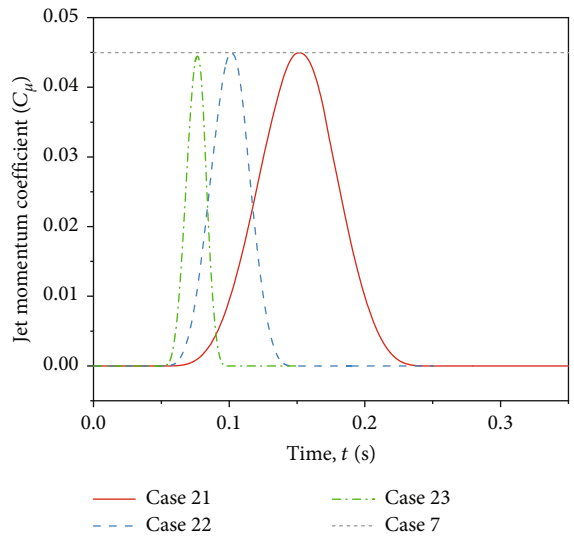

Figure 12: Time history curves of jet momentum coefficient in discrete gust cases.

angle, which is defined as $A = \arctan(u_y/u_x)$, where u_x and u_y represent the local x and y velocity components, and $A < 0$ means that the vertical velocity component is pointing the negative y direction. The term gust angle is used below for ease of expression, and its absolute value rather than the actual value is used to represent the deflection angle. As shown in Figure 9, the y velocity contour and gust angle isoline of case 9 are shown. In general, the flow deflection caused

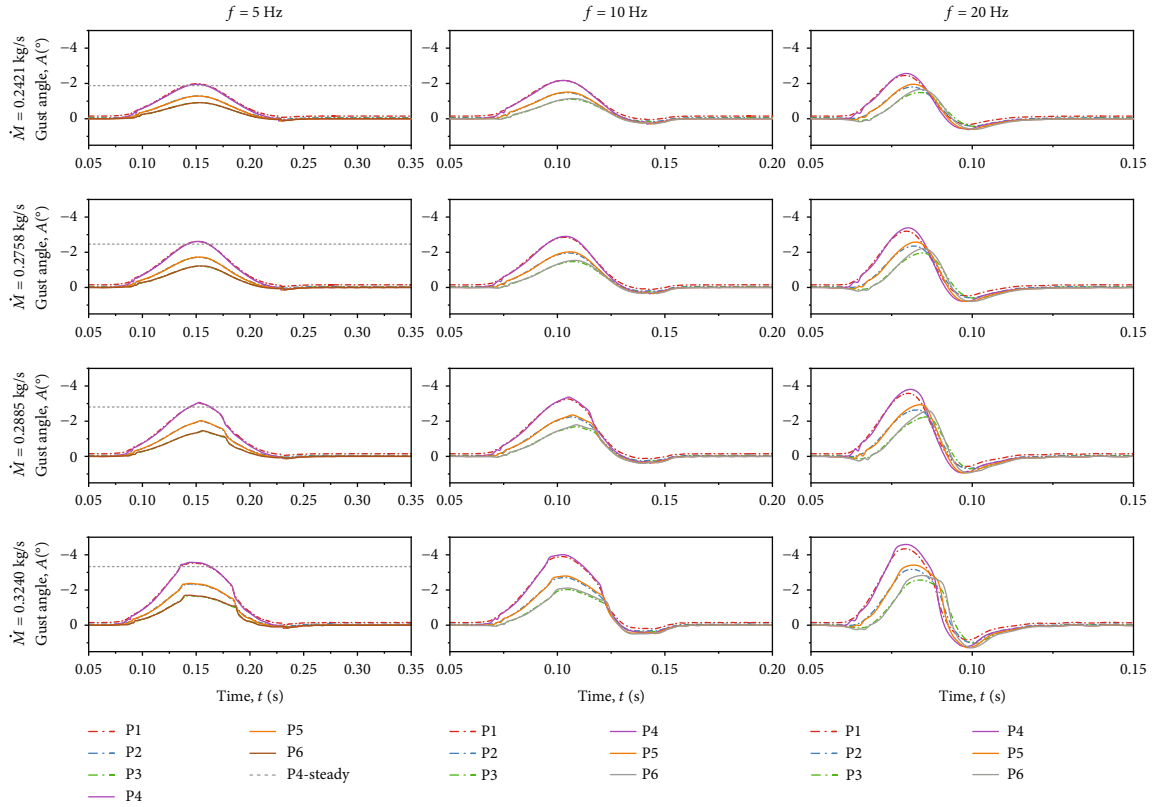

Figure 13: Time history curves of gust angle in discrete gust cases.

by the trailing jet decays obviously along the streamwise direction, while it varies nonuniformly in the wake area due to the influence of the shear layer.

There are 9 monitoring points (P1 to P9) setting at 2c, 3c, and 4c away from the vane tail in a streamwise direction, as presented in Figure 4. Figure 10 shows the changes in the gust angle at these monitoring sites with jet intensity. The coordinates of the positions are given in the figure, with the coordinate origin located at the half-chord length of the vane. At the same x position, the gust angles at $y = 0$ and $0.5c$ are very close, while the data at $y = -0.5c$ is smaller than that at the other two positions. The difference between them hardly changes with jet intensity but gradually decreases with the increase of streamwise distance. Observing the figure, it is found that there are two obvious linear relationships between the gust angle and jet momentum coefficient. As shown in Figures 7(a) and 7(b), the first six groups of data correspond to the flow state that the jet separation position changes with the jet momentum. When $C_\mu > 0.0401$, the jet separates from a fixed position, and the slope of the curve in the figure increases slightly. However, this change is less significant as the streamwise distance increases. Earlier studies on the circulation control airfoil point out [29] that the relationship between the aerodynamic performance of airfoils and jet momentum coefficient can be divided into two stages, separation control zone, and supercirculation control zone. The difference between them is mainly reflected in the different control efficiency of the jet on the lift coefficient. This phenomenon is believed to be caused by the jet separation position on the trailing edge profile and the interaction of the jet and the oncoming flow. As the blowing increases, the flow near the wall is entrained and mixed with the Coanda jet. The separated jet penetrates the low-energy wake region and induces streamline deflection. Combined with the numerical results in this section, it can be inferred that there is a similar piecewise relationship between the flow deflection caused by steady blowing and the jet intensity. The first linear stage is mainly caused by the jet separation position on the trailing edge, which depends on the blowing strength. However, when the jet separation position is fixed and no longer changes as the jet momentum increases, the interaction of the jet and the oncoming flow is the major factor leading to the different slopes of the latter part of the curve.

3.1.2. Unsteady Jet Results. Figure 11 shows the transient contours of the gust angle in case 23, where the jet duration is 0.05 s. The gust angle is first positive in the downstream area when the trailing edge blowing starts. Then, it turns to negative, which indicates the expected deflection direction, as the upstream disturbance propagates. We can see the sudden change in the gust angle near the centerline. This is one of the reasons why paired devices are usually used in wind tunnels because the distortion of the local flow field will occur at the position on the path of the unsteady jet wake.

The variation curves of C_μ in case 21~23 are plotted in Figure 12, including a grey line indicating the value in case 7. The mass flow rate amplitudes are the same in these cases. Although we did not directly specify the jet momentum

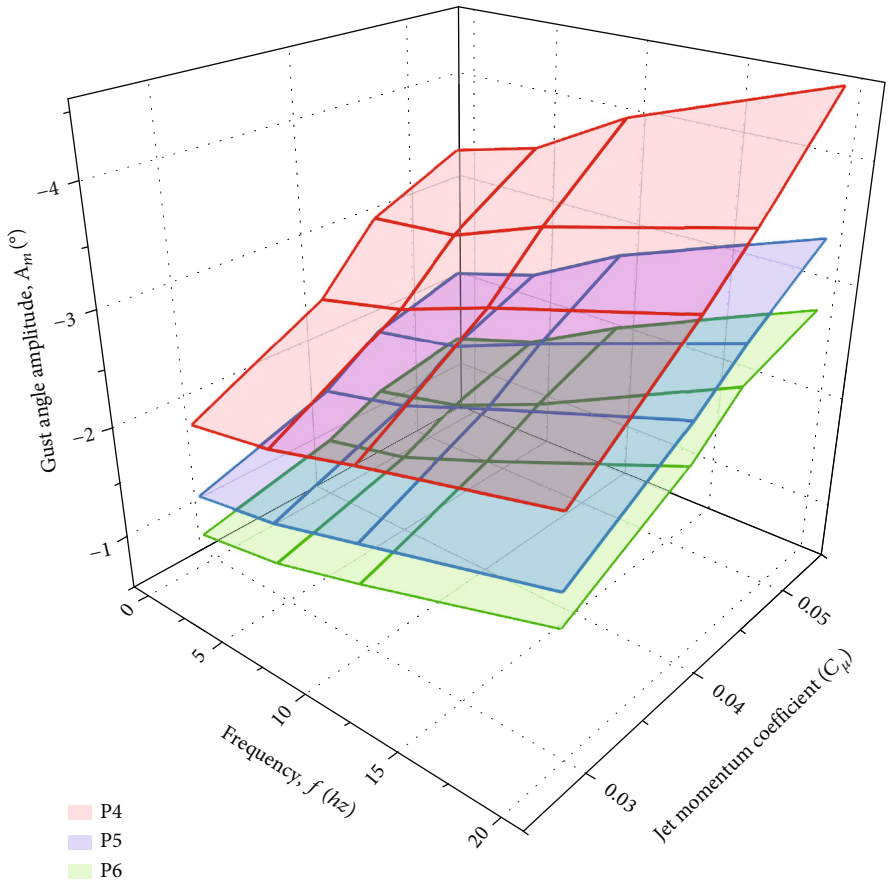

Figure 14: Results of gust angle amplitude in discrete gust cases.

coefficient as the inlet condition, the curve maintains a smooth pulse shape similar to the "1-cos" profile. The data shows that at 5 Hz and 10 Hz, the amplitude of the unsteady jet momentum coefficient is equal to that in the steady jet case, while the value at 20 Hz is 1% less. Due to the simple configuration of the internal channel, the loss of momentum with frequency is not obvious here.

The time history curves of gust angle at P1~P6 in cases 15~26 are presented in Figure 13. Obviously, the amplitude of the gust angle increases with the increase of frequency and jet momentum coefficient. Taking the data at P4 as an example, the amplitudes in cases 15~17 are 1.95°, 2.17°, and 2.57°, which are 4.02%, 15.76%, and 37.09% higher than that of the steady case, respectively. Furthermore, there is a difference in the amplitude at different vertical positions due to the unsteady effect of high frequency. Figure 14 plots the peak values of the gust angle curve at P4~P6 in all discrete gust cases.

Figure 13 also shows the difference in gust shape among the cases with different jet intensity. When the amplitude of C_μ is small, the symmetry and smoothness of the gust shape are good, especially near the peak. With the increase in frequency, the curve will be more inclined in the initial stage of jet enhancement. That is the peak hysteresis caused by the unsteady effect, similar to the phenomenon in unsteady aerodynamics. However, when the amplitude of the C_μ is large, as presented in the lower part of the figure, curves are unsmooth and asymmetric with two turning points, even at low frequencies. This is undesirable for the target of simulating the "1-cos" shape accurately.

The inlet conditions of case 15~20 correspond to the state that the jet does not completely flow over the trailing edge in the steady cases. Case 21~26 corresponds to the state where the jet separation position is fixed. Combined with the previous results, it can be considered that the different deflection efficiency in the above two flow states leads to the unsmooth and segmented curves of the gust angle. The critical amplitude of the jet momentum coefficient is about 0.0401~0.0450 in this study.

The gust angle and jet momentum coefficient data at the monitoring point P5 when gust frequencies equal 5 Hz and 20 Hz are extracted, respectively. After amplitude normalization and starting time alignment, the change of gust shape can be seen more clearly, as shown in Figure 15. It shows that the gust shape is more similar to the jet momentum coefficient curve than the standard "1-cos" shape, which is also the profile of the mass flow rate. In order to quantify the similarity of waveforms, cross-correlation calculation is performed between the gust profile and the other two curves according to Eqs. (7) and (8), and normalized cross-correlation coefficients are obtained. The results are shown in Table 5, where $\hat{r}_{gs}$ represents the cross-correlation coefficient between the gust shape and the "1-cos" curve, and

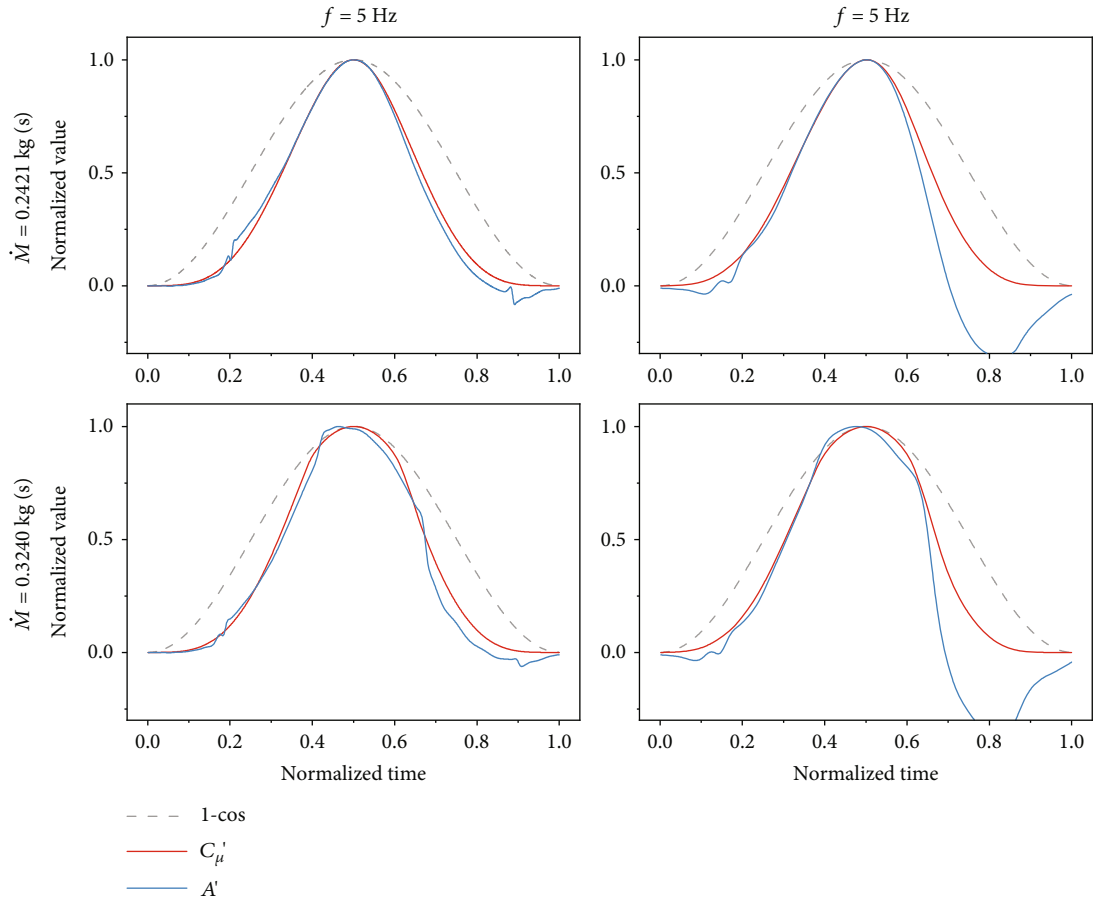

Figure 15: Normalized curves of gust angle and jet momentum coefficient.

$\hat{r}_{gm}$ represents the coefficient between the gust shape and the C_μ curve.

$$r_{xy}(j) = \sum_{i=1}^{N-j-1} x(i)y(i-j), \tag{7}$$

$$r_{xy,n}(j) = \frac{r_{xy}(j)}{\sqrt{r_{xx}(0)r_{yy}(0)}}. \tag{8}$$

As can be seen, the cross-correlation coefficient $\hat{r}_{gm}$ can reach over 0.94, while $\hat{r}_{gs}$ drops to a minimum of 0.86. Based on the data variation, the increase in frequency has a greater impact on the calculation results than the impact of jet momentum. This reveals that the control of the jet momentum coefficient curve plays a key role in accurately simulating the gust shape. Since the jet momentum cannot be directly controlled in the experiment, the corresponding relationship between it and the mass flow rate in the plenum chamber needs to be found by measuring the jet velocity at the slot.

In addition, the reverse rise at the beginning and the ending of gust profiles can be found, corresponding to the red contour area in Figure 11. The response amplitude to this effect appears to be different at different locations. The longer the streamwise distance is, the greater the influence in the initial stage is. According to Ref. [18], the reverse increase of the gust angle seen in the figure is mainly caused by the starting vortex and the stopping vortex created when generating and losing lift on the vane, induced by the change of circulation through the starting and cessation of blowing. And this is also the main reason for the decrease in the cross-correlation coefficient at high jet frequencies. To get a more ideal gust shape, this influence might be reduced by decreasing the vorticity at the gust's beginning and end in an appropriate way [12].

Table 5: Cross-correlation coefficient of normalized curves.

Case	$\dot{M}_{2D}$ (kg/s)	f (Hz)	$\hat{r}_{gs}$	$\hat{r}_{gm}$
15	0.2421	5	0.9624	0.9986
17	0.2421	20	0.8695	0.9518
24	0.3240	5	0.9578	0.9968
26	0.3240	20	0.8654	0.9459

3.2. Results with Wind Tunnel Sidewalls

3.2.1. Blowing Activation Ratio = 100%. Firstly, the 3D flow patterns with all blowing activation under different gust

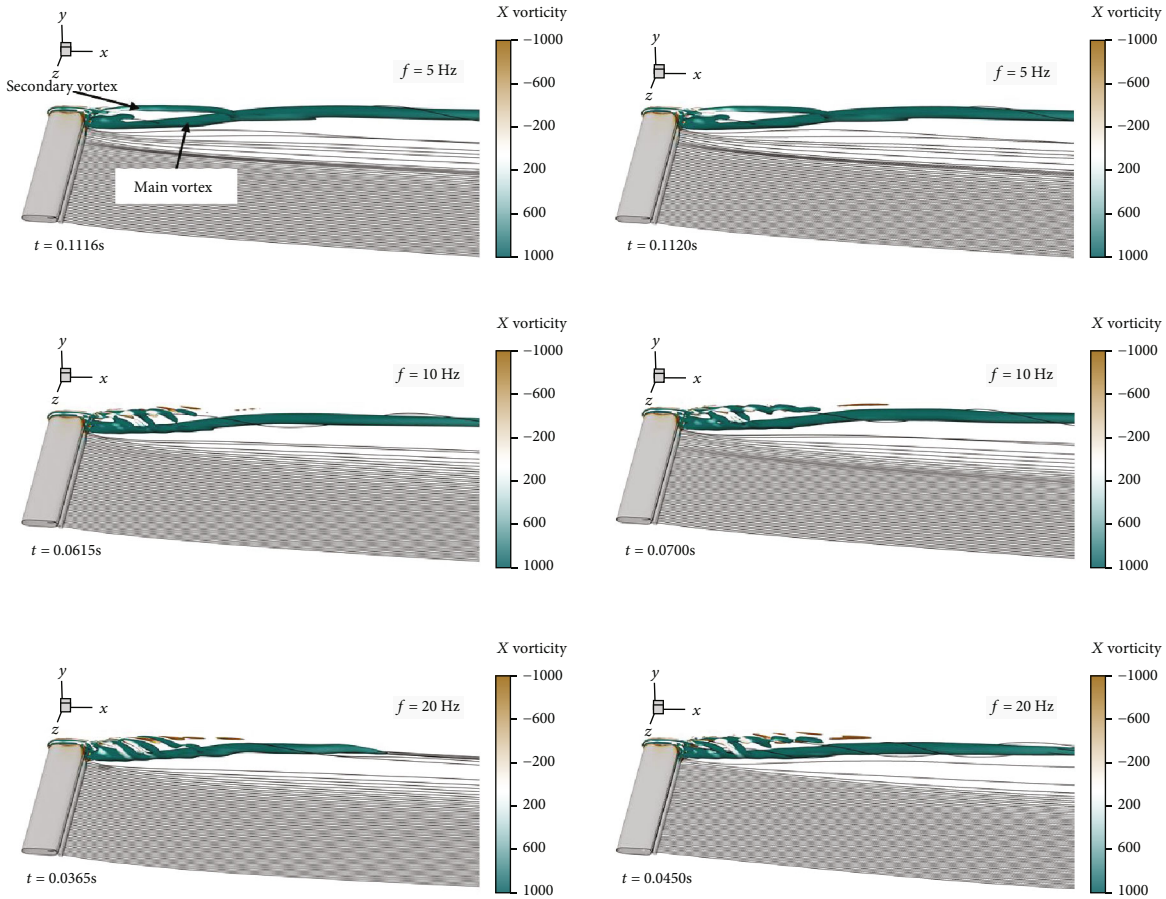

Figure 16: Transient vortical structure near the sidewall and streamlines starting from the jet slot.

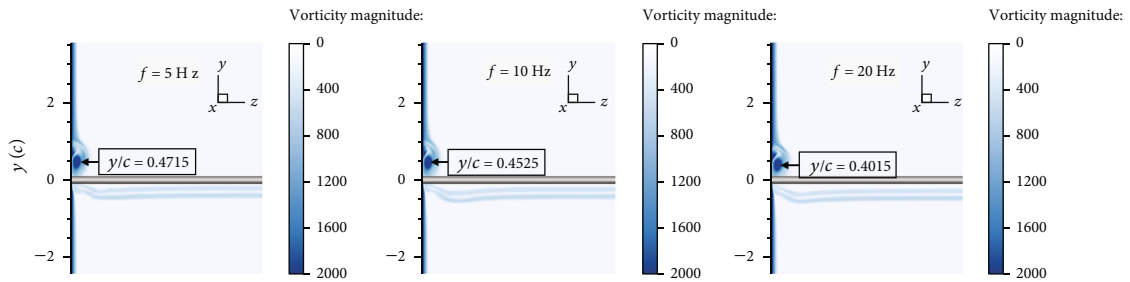

Figure 17: Transient vorticity magnitude contours under different jet frequencies.

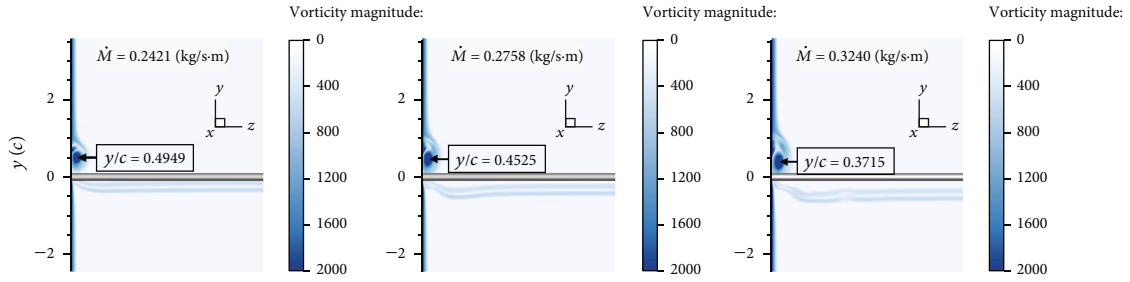

Figure 18: Transient vorticity magnitude contours under different jet mass flow rate.

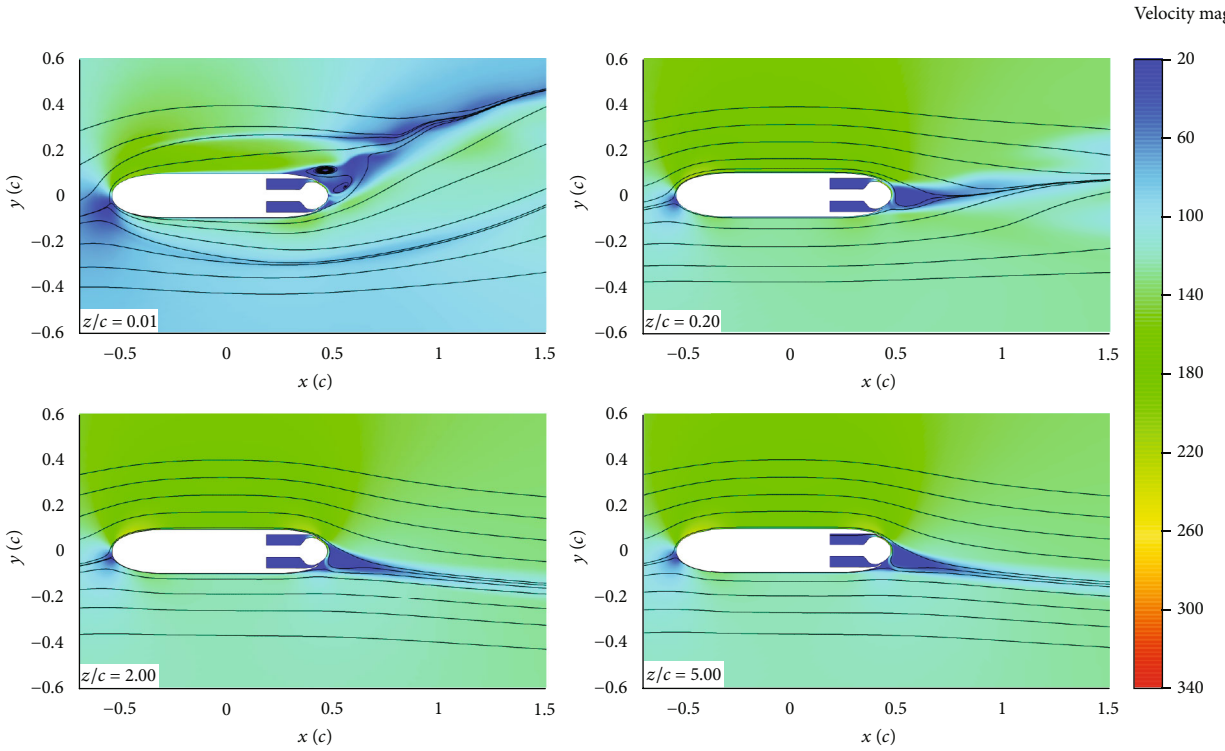

(a) Velocity contours and streamlines

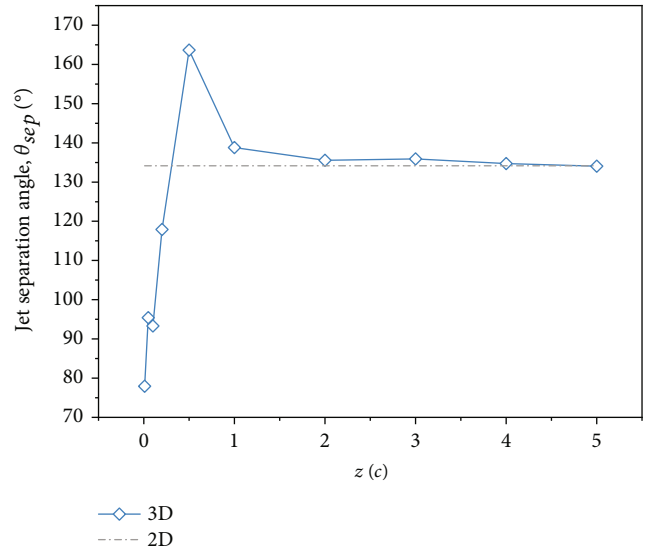

(b) Spanwise variation of jet separation angle

FIGURE 19: Typical transient flow field and jet separation angles at different spanwise positions in 3D simulation.

frequencies are analysed. Figure 16 shows the streamlines starting from the trailing edge jet slot at the moments when C_μ is maximum and the gust angle at the position ($x = 5c$, $y = 0$, $z = 5c$) reaches the peak. The corresponding time information is written in the graph. The streamwise vortical structure is marked with the positive Q criterion isosurface and colored with x vorticity. There are obvious vortices near the sidewall, which can be divided into two parts according to the mode. The first part is the main vortex, which extends longer in the streamwise direction. The other vortex is closer to the wall, has a smaller vorticity, and breaks down under high-frequency jets. According to the indication of the streamlines, the main vortex is formed by the rolling up of the Coanda jet and rises in the opposite direction due to the induced velocity. The secondary vortex is formed by the interaction between the sidewall boundary layer and the vane's end and is affected by the main vortex.

It is reasonable to assume that the main vortex will have a positive effect on gust intensity. The x vorticity contour indicates that the main vortex is oriented in the $+x$ direction.

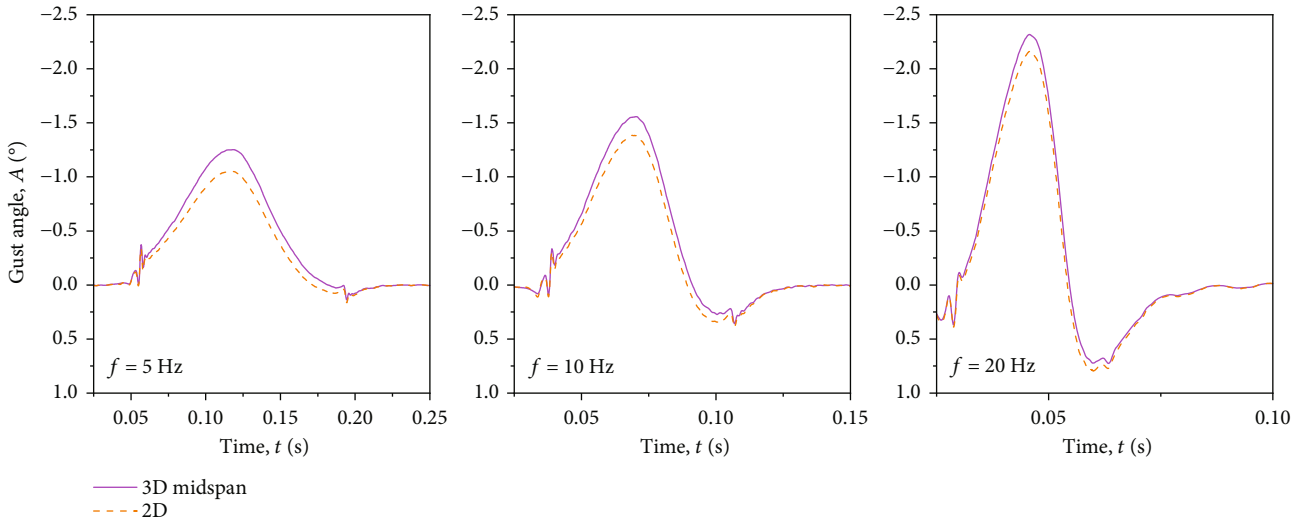

Figure 20: Time history curves of gust angle in 2D and 3D simulations.

The rotating direction is clockwise while observing along the flow. As a result, the influence of the main vortex on the deflection of streamlines is consistent with that of the Coanda jet. However, the secondary vortex breaks down along the stream. The rotating direction of the part near the sidewall is opposite to the main vortex, while the part entrained by the main vortex is in the same direction as the main vortex.

Consistent with the results of steady blowing [22], the flow at most spanwise locations near the midspan plane is quasi two-dimensional. At the same time, it can be clearly seen that the influence of the main vortex on the mainstream is reflected in the spanwise variations of the shape streamlines. When $f = 5$ Hz, there is no significant change in the flow between these two moments, and a clear interface can be seen in the streamlines. When $f = 10$ Hz, it gradually shows the influence of vortex on the streamlines. While when $f = 20$ Hz, the impact of the vortex on the streamlines of the mainstream region is hardly ever seen. This indicates that the low jet frequency produces sufficient time for the development of the sidewall vortex, thereby exacerbating the impact on the main flow.

The vorticity magnitude contours of the $x = 5c$ plane are presented in Figure 17, showing the distribution of sidewall vortices and jet wake. The vertical position of the jet wake represents the degree of flow deflection, which is consistent with the 2D flow. The lower it is, the bigger the gust angle is. The vertical distance of the sidewall main vortex also varies at various frequencies. The vortex core is located closer to the central plane ($y = 0$) in the high-frequency solution. The reason for this difference may be that the flow deflection caused by the Coanda jet can also affect the reverse-induced velocity of the sidewall vortices, limiting its development. At high frequencies, the gust angle is bigger, so this limitation is more apparent.

Figure 18 shows the results under different mass flow rate amplitudes. Similarly, the vertical distance of the main vortex on the sidewall decreases with the increase of gust

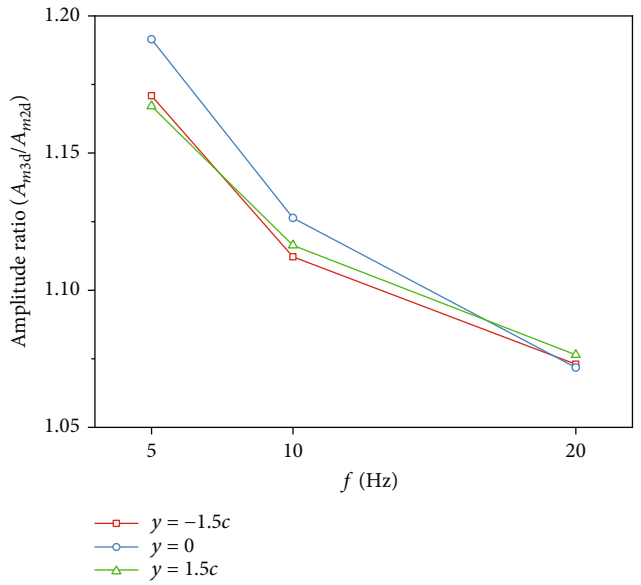

Figure 21: Comparison of gust angle amplitude between 2D and 3D simulations.

Table 6: Comparison of jet momentum coefficient between 2D and 3D simulations.

Case	f (Hz)	Dimension	C_μ
18	5	2D	0.0401
39	5	3D (midspan)	0.0402
		3D (whole)	0.0351
19	10	2D	0.0401
40	10	3D (midspan)	0.0402
		3D (whole)	0.0352
20	20	2D	0.0398
41	20	3D (midspan)	0.0400
		3D (whole)	0.0349

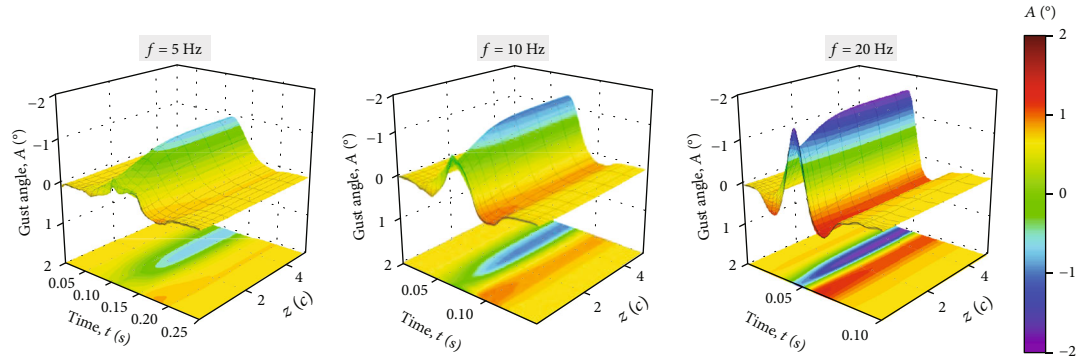

(a) Results of the monitoring line ($y = -1.5c$)

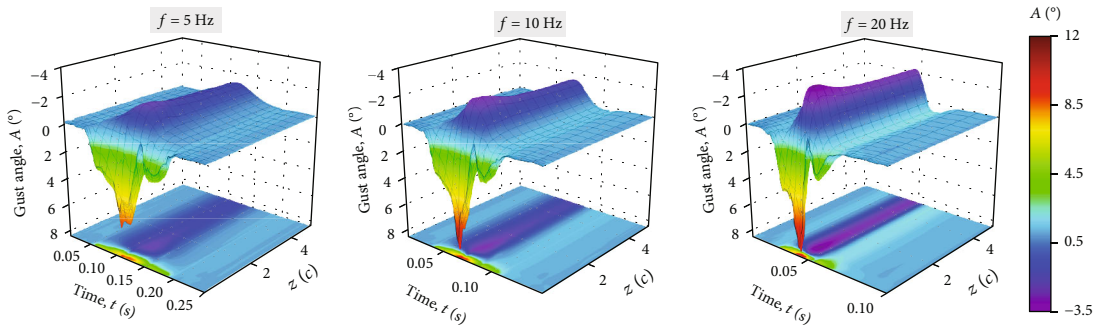

(b) Results of the monitoring line ($y = 0$)

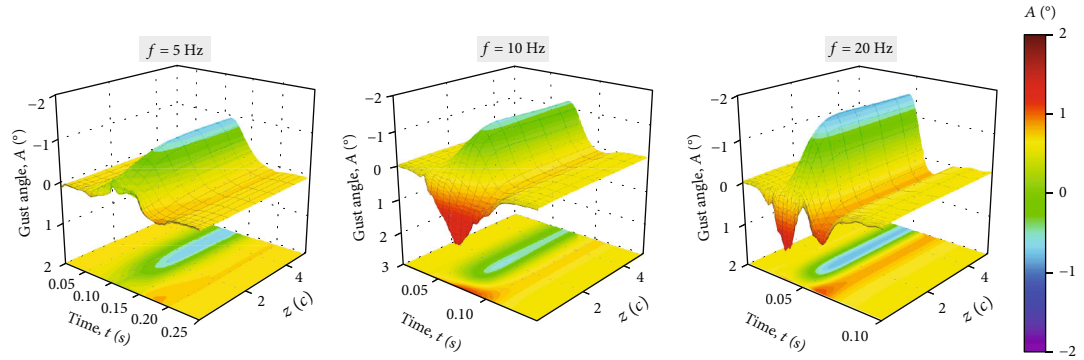

(c) Results of the monitoring line ($y = 1.5c$)

FIGURE 22: Time variation of gust angle on the monitoring line.

angle. This confirms the above speculation that sidewall vortices interact with gusts in the mainstream.

Firstly, the distinctions between 2D and 3D simulations are studied by comparing the flow patterns. Figure 19 shows the transient velocity contours and jet separation angles at different spanwise positions in case 39 at $t = 0.112$ s. Compared to the 2D solution, the spanwise variation of the flow demonstrates the complex 3D characteristics of this solution, especially in the near-wall region. At $z = 0.01c$ (0.1% span), the front stagnation location is away from the vane surface, and the jet curls up after separation. At $z = 0.2c$ (2% span), the front stagnation point is found on the surface of the vane. The flow at $z = 2.5c$ (25% wingspan) and $5.0c$ (50% span) is basically consistent with the 2D results, and the jet continues to penetrate the flow field downward after separation. These results are similar to the findings in Ref [22]. The jet separation angles at different spanwise locations are plotted in Figure 19(b). When $z < 0.5c$ (5% span), θ_{sep} is smaller than the midspan result and increases along the spanwise. θ_{sep} reaches its maximum near $z = 0.5c$ and is greater than the midspan and 2D results. Between $z = 2.0c$ (20% span) and $5.0c$, θ_{sep} remains almost unchanged, approximately equal to the 2D result. This indicates that the influence of streamwise vortices on the flow of the Coanda jet is mainly concentrated within the 20% span range near the sidewall.

Next, we compare the generation of gusts to further illustrate the differences between 2D and 3D simulations. The time history curves of the gust angle at the position ($x = 5c$, $y = 0$) are shown in Figure 20. Under different gust durations, the shapes of the two corresponding curves are very similar, but the peaks are slightly different. For the convenience of observation, the gust angle amplitude ratios of

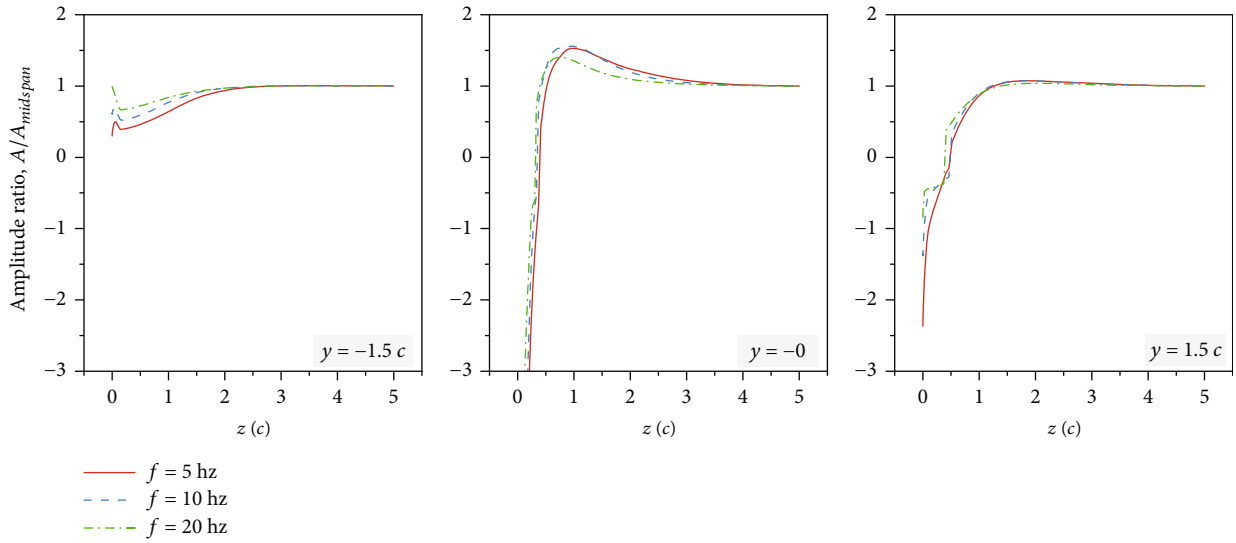

Figure 23: Time variation of gust angle on the monitoring line.

3D and 2D results are extracted and presented in Figure 21. Three vertical positions were selected considering the effect of the relative position to the vortex, including $y = 0$, -1.5c, and 1.5c. The gust angle amplitude in the 3D case is slightly larger than that in the 2D case, with the ratio getting smaller as the frequency increases. Table 6 lists the peak of C_μ for the corresponding cases, including the midspan results and the whole span results from the same 3D solution. It is evident that the 2D and 3D midspan results are almost the same, while the whole span results decrease due to the sidewall effect. This implies that the vortex rolled up on the sidewall has almost no influence on the Coanda jet in the midspan plane. Therefore, it also demonstrates that the amplification of gust amplitude at midspan is mainly due to the downwash in the downstream flow field caused by sidewall vortices.

Next, the spanwise distribution of gusts caused by sidewall effects is analysed by comparing the temporal and spatial characteristics of the gust angle at different jet frequencies. The gust angle results of the three monitoring lines in the $x = 5c$ plane are shown in Figure 22. In general, the gust amplitude distribution is uniform near the midspan plane, and good phase synchronization is maintained. However, it should be noted that the sidewall vortices have different effects at different vertical positions. For both vertical distances above the centerline, the flow near the sidewall follows the opposite direction of the expected gust, but the reverse peak value varies inversely with gust frequency. This should be related to the change in the vertical position of the vortices. As the frequency increases, the sidewall vortices move downward, closer to the monitoring line ($y = 0$), so its reverse flow angle is larger. Meanwhile, this value of the monitoring line ($y = 1.5c$) is smaller, because the vortex is farther away. As for the monitoring line ($y = -1.5c$), it seems that the influence of sidewall vortices is no longer dominant, and there is no reverse flow.

In order to compare the spanwise uniformity at different frequencies more directly, the results of the gust amplitude ratio are shown in Figure 23, with the value at the midspan set to 1. Table 7 lists the spanwise ranges where the amplitude deviation is within 10%. Although the difference of the monitoring line ($y = 1.5c$) is not significant, it can still be concluded that the span uniformity is worst at the gust frequency of 5 Hz.

Table 7: Results of spanwise uniformity.

Vertical position	f (Hz)	Spanwise range
$y = -1.5c$	5	64.2%
	10	70.6%
	20	73.6%
$y = 0$	5	43.8%
	10	50.4%
	20	60.6%
$y = 1.5c$	5	79.0%
	10	80.0%
	20	79.4%

Before the gust response test, measurements of gust in the wind tunnel are required to assess gust strength, shape, and spatial uniformity. From the above results, the situation that has the greatest impact on the spanwise distribution is the low-frequency blowing, which requires special attention. We speculate that while the sidewall streamwise vortex promotes the gust amplitude, its influence range is likewise restricted by the gust because the induced velocity of the vortex itself is opposite to the gust velocity. At high blowing frequencies, this limitation is more obvious due to the greater gust velocity.

3.2.2. Blowing Activation Ratio = 85%. Moreover, Ref. [18, 19] mentioned that the trailing edge blowing at the vane end was inactive during the test to avoid the gust being damped

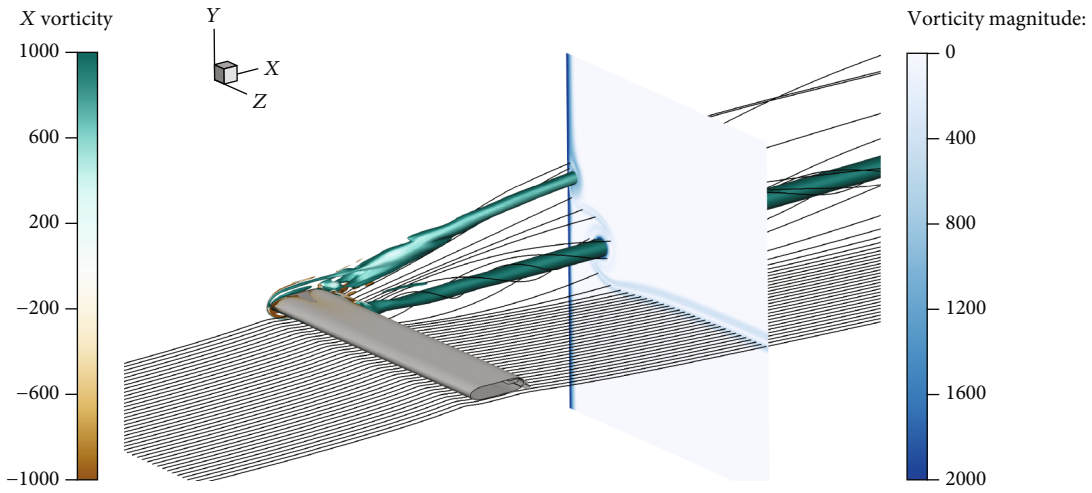

Figure 24: Transient vortical structure, streamlines, and vorticity magnitude contours when blowing activation ratio is 85%.

out in too short a distance downstream of the rig vanes. However, the motivations and functions of this approach have not been publicly demonstrated before. In order to reveal the mechanism, the flow with blowing partially activated was simulated in this section. The jet is not open in the 15% of the vane near the sidewall. Figure 24 presents the transient vortical structure, streamlines, and vorticity magnitude contours at $t = 0.07$ s, corresponding to Figure 16. Two vortices can be clearly found, located near the sidewall and at the end of trailing edge blowing. According to streamlines, the air flowing opposite to the gust is generated in over 15% of the spanwise region due to these two vortices.

A comparison of the gust of cases 40 and 44 is provided below to demonstrate the effect of partially closing the blowing at the vane's end. When setting the inlet conditions of case 44, adjust the total mass flow rate amplitude to ensure the same value per unit spanwise length. The results show that the jet momentum coefficients at the midspan plane of these two cases are almost equal, with values of 0.0402 and 0.0401, respectively. This difference is small enough that the comparison between the two simulations is meaningful.

Figure 25 shows the spanwise distributions of gust angle amplitude of the monitoring line ($x = 5c$, $y = 0$). In most regions near the midspan plane, the gust amplitude obtained in case 44 is larger. The values at the midspan plane are 2.18° and 1.56°, an increase of approximately 40%. This amplification effect is significant. However, severe spanwise nonuniformity occurs near the position where the jet stops, due to the influence of the main vortex. After simple calculations, the range where the amplitude deviation is within 10% only covers 33.1% span length.

The main vortex formed by the jet sheet curling has a greater impact on the mainstream gust as it moves away from the sidewall. It not only increases the amplitude of gusts, thereby avoiding rapid fading along the flow path, but also reduces the mass flow rate demand for blowing. Nevertheless, this cross-flow vortex generates a varied cross-plane velocity distribution that results in the gust amplitude variation along the typical model span. Therefore, in the experiment, it is necessary to adjust the spanwise distribution of mass flow rate or plenum pressure to achieve uniform gusts in the model area according to the test requirements.

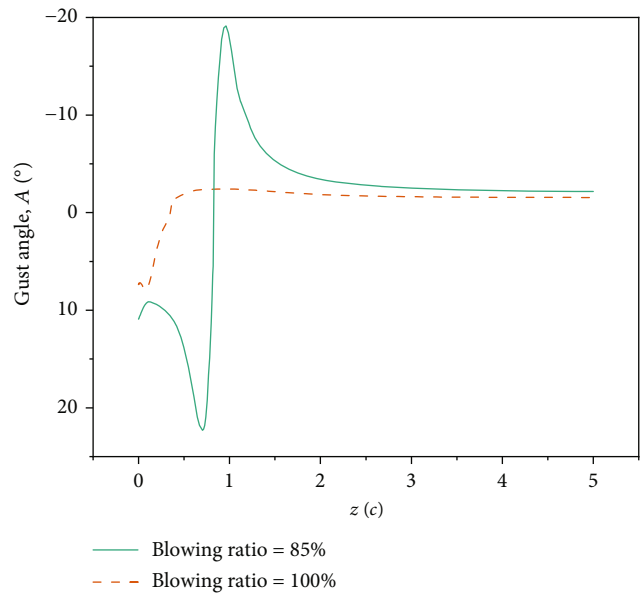

Figure 25: Comparison of the spanwise distribution of gust angle amplitude between different blowing activation ratios.

4. Conclusions

In this paper, the flow around a new type of gust generator has been numerically simulated to verify the discrete gust generation ability of trailing edge blowing under subsonic inflow. Results preliminarily reveal the influence of jet control parameters on gust characteristics and verify the effectiveness of partial spanwise blowing on increasing gust amplitude. Specifically, the following conclusions are obtained.

The frequency and momentum of unsteady jets are the main factors affecting discrete gust characteristics. Firstly, the higher the jet frequency, the greater the amplitude of the gust angle due to unsteady effects. In this study, the

5 Hz jet induces a quasisteady gust with a less than 5% variation in amplitude from the steady result, while the 20 Hz jet increased the amplitude by 37%. Secondly, an increase in jet frequency could result in reverse peaks at the beginning and end of the jet, which causes discrepancies between the generated and expected gust shapes. The gust amplitude is also positively correlated with the jet momentum. There is a critical value where the gust shape is smooth when the jet momentum is less than this value, and cusps appear on the profile when it is greater than this value. This is because while the jet momentum is large, the farthest separation position on the trailing edge remains fixed, which changes the efficiency of the jet in deflecting the flow.

When considering the tunnel sidewall, the jet sheets near the sidewall roll up to form a downstream vortex. The vortex exhibits interactions with the generated discrete gusts. On the one hand, the presence of the downwash results in an increase of about 10% to 20% in the gust amplitude on the symmetric plane, when compared to the 2D results. And the spatial nonuniformity is generated. On the other hand, the flow deflection caused by blowing can change the position of the streamwise vortex core, resulting in differences in the impact on the mainstream under different jet conditions.

Moreover, the impact mechanism of partially spanwise blowing on gusts is revealed. When the activation ratio of spanwise blowing is limited to 85%, streamwise vortices are formed at both the sidewall and the spanwise position where the blowing stops. Due to the main vortex being closer to the mainstream, the gust amplitude at the symmetry plane has increased by nearly 40%. This result provides a physical explanation for the availability of this operation to reduce gust attenuation. Although it may exacerbate the spanwise nonuniformity of gust amplitude, the application of this method remains beneficial in practice.

Nomenclature

A: Gust angle
c: Chord length
C_{rc}: Rotation and curvature correction factor
C_μ: Jet momentum coefficient
F_1, F_4: Auxiliary function in turbulence model
F_j: Thrust generated by jet
k: Kinetic energy of turbulence
$\dot{m}$: Mass flow rate
$\dot{M}$: Amplitude of mass flow rate
p: Pressure
P: Production of kinetic energy of turbulence
q: Dynamic pressure
$\hat{r}_{gs}$, $\hat{r}_{gm}$: Normalized cross-correlation coefficient
R_i: Richardson number
R: Gas constant
t: Time
T: Temperature
u: Velocity
xj: Cartesian coordinates
β, β^*: Turbulence model coefficients
γ: Specific heat ratio
θ_{sep}: Jet separation angle
μ: Dynamic viscosity
ρ: Density
σ_k, σ_ω: Turbulence model coefficients
ω: Specific dissipation of turbulence kinetic energy.

Data Availability

The computational data used to support the findings of this study are available from the corresponding author upon request.

Conflicts of Interest

The authors declare that they have no known competing financial interests or personal relationships that could have appeared to influence the work reported in this paper.

Acknowledgments

This research was partially supported by the Natural Science Foundation of Sichuan (No. 2023NSFSC0400).

References

[1] A. R. Jones, O. Cetiner, and M. J. Smith, "Physics and modeling of large flow disturbances: discrete gust encounters for modern air vehicles," *Annual Review of Fluid Mechanics*, vol. 54, no. 1, pp. 469–493, 2022.

[2] S. Guo, J. Los, and Y. Liu, "Gust alleviation of a large aircraft with a passive twist wingtip," *Aerospace*, vol. 2, no. 2, pp. 135–154, 2015.

[3] C. An, C. Yang, C. Xie, and Y. Meng, "Gust load alleviation including geometric nonlinearities based on dynamic linearization of structural ROM," *International Journal of Aerospace Engineering*, vol. 2019, Article ID 3207912, 20 pages, 2019.

[4] Y. Zhou, Z. Wu, and C. Yang, "Gust alleviation and wind tunnel test by using combined feedforward control and feedback control," *Aerospace*, vol. 9, no. 4, pp. 225–227, 2022.

[5] Y. Liu, C. Xie, C. Yang, and J. Cheng, "Gust response analysis and wind tunnel test for a high-aspect ratio wing," *Chinese Journal of Aeronautics*, vol. 29, no. 1, pp. 91–103, 2016.

[6] P. M. G. J. Lancelot, J. Sodja, N. P. M. Werter, and R. D. Breuker, "Design and testing of a low subsonic wind tunnel gust generator," *Advances in Aircraft and Spacecraft Science*, vol. 4, no. 2, pp. 125–144, 2017.

[7] D. M. Tang, P. G. A. Cizmas, and E. H. Dowell, "Experiments and analysis for a gust generator in a wind tunnel," *Journal of Aircraft*, vol. 33, no. 1, pp. 139–148, 1996.

[8] J. Neumann and H. Mai, "Gust response: simulation of an aeroelastic experiment by a fluid-structure interaction method," *Journal of Fluids and Structures*, vol. 38, pp. 290–302, 2013.

[9] V. Brion, A. Lepage, Y. Amosse et al., "Generation of vertical gusts in a transonic wind tunnel," *Experiments in Fluids*, vol. 56, no. 7, pp. 145–170, 2015.

[10] J. J. Gilman and R. M. Bennett, "A wind-tunnel technique for measuring frequency-response functions for gust load analyses," *Journal of Aircraft*, vol. 3, no. 6, pp. 535–540, 1966.

[11] R. C. Scott, T. K. Vetter, K. B. Penning, D. A. Coulson, and J. Heeg, "Aeroservoelastic testing of a sidewall mounted free

flying wind-tunnel model," in *26th AIAA Applied Aerodynamics Conference*, Honolulu, Hawaii, USA, 2008.

[12] D. Balatti, H. H. Khodaparast, M. I. Friswell, and M. Manolesos, "Improving wind tunnel '1-cos' gust profiles," *Journal of Aircraft*, vol. 59, no. 6, pp. 1514–1528, 2022.

[13] Q. Sun, Z. Shi, W. Zhang, Z. Sun, and Y. Chen, "Numerical simulation of ground effect on circulation control airfoil," *International Journal of Aerospace Engineering*, vol. 2022, Article ID 4985193, 20 pages, 2022.

[14] Y. Chen, Z. Hou, X. Deng, Z. Guo, S. Shao, and B. Xu, "Numerical study of the lift enhancement mechanism of circulation control in transonic flow," *Aerospace*, vol. 8, no. 11, p. 311, 2021.

[15] L. Zhang, Y. Huang, Z. H. Zhenglong et al., "Virtual flight test of pitch and roll attitude control based on circulation control of tailless flying wing aircraft without rudders," *Chinese Journal of Aeronautics*, vol. 36, no. 6, pp. 52–62, 2023.

[16] Y. Li and N. Qin, "A review of flow control for gust load alleviation," *Applied Sciences*, vol. 12, no. 20, article 10537, 2022.

[17] A. Jones, A. Edstrand, M. Chandran, D. Wetzel, F. Liu, and L. Cattafesta, "An experimental investigation of unsteady and steady circulation control for an elliptical airfoil," in *48th AIAA Aerospace Sciences Meeting Including the New Horizons Forum and Aerospace Exposition*, Orlando, Florida, USA, 2010.

[18] N. J. Allen and M. K. Quinn, "Development of a transonic gust rig for simulation of vertical gusts on half-models," *Journal of Aircraft*, vol. 52, no. 3, pp. 535–540, 2015.

[19] A. Gomariz-Sancha, A. J. Peace, D. A. Roberts, and T. S. C. Davidson, "Towards the industrialisation of a transonic gust rig for simulation of gusts on half-models," in *2018 AIAA Aerospace Sciences Meeting*, Kissimmee, Florida, USA, 2018.

[20] C. Easa, *Certification Specifications for Large Aeroplanes, Cs 25*, EASA, 2009.

[21] Z. Wu, Y. Cao, and M. Ismail, "Gust loads on aircraft," *The Aeronautical Journal*, vol. 123, no. 1266, pp. 1216–1274, 2019.

[22] T. Nishino and K. Shariff, "Numerical study of wind-tunnel sidewall effects on circulation control airfoil flows," *AIAA Journal*, vol. 48, no. 9, pp. 2123–2132, 2010.

[23] M. Lone and G. Dussart, "Impact of spanwise non-uniform discrete gusts on civil aircraft loads," *The Aeronautical Journal*, vol. 123, no. 1259, pp. 93–120, 2019.

[24] Y. Yang, C. Yang, and Z. Wu, "Aeroelastic dynamic response of elastic aircraft with consideration of two-dimensional discrete gust excitation," *Chinese Journal of Aeronautics*, vol. 33, no. 4, pp. 1228–1241, 2019.

[25] C. L. Rumsey and T. Nishino, "Numerical study comparing RANS and LES approaches on a circulation control airfoil," *International Journal of Heat and Fluid Flow*, vol. 32, pp. 847–864, 2011.

[26] A. Hamed, "Some improvements in Menter's k-omega SST turbulence model," in *29th AIAA Fluid Dynamics Conference*, Albuquerque, New Mexico, USA, 1998.

[27] M. Mani, J. A. Ladd, and W. W. Bower, "Rotation and curvature correction assessment for one-and two-equation turbulence models," *Journal of Aircraft*, vol. 41, no. 2, pp. 268–273, 2004.

[28] R. J. Englar, G. S. Jones, B. Allan, and J. Lin, "2-D circulation control airfoil benchmark experiments intended for CFD code validation," in *47th AIAA Aerospace Sciences Meeting Including the New Horizons Forum and Aerospace Exposition*, Orlando, Florida, USA, 2009.

[29] G. Jones, C. Yao, and B. G. Allan, "Experimental investigation of a 2D supercritical circulation-control airfoil using particle image velocimetry," in *3rd AIAA Flow Control Conference*, San Francisco, California, USA, 2006.